Lab on a Chip

PAPER

View Article Online
View Journal | View Issue

Cite this: *Lab Chip*, 2024, **24**, 4461

Integration of complementary split-ring resonators into digital microfluidics for manipulation and direct sensing of droplet composition†

Dipesh Aggarwal, [ab] Richard Piffer Soares de Campos, [a] Abebaw B. Jemere, [ac] Adam Johan Bergren [ad] and Nikola Pekas *[a]

This paper demonstrates the integration of complementary split-ring resonators (CSSRs) with digital microfluidics (DMF) sample manipulation for passive, on-chip radio-frequency (RF) sensing. Integration is accomplished by having the DMF and the RF-sensing components share the same ground plane: by designing the RF-resonant openings directly into the ground plane of a DMF device, both droplet motion and sensing are achieved, adding a new on-board detection mode for use in DMF. The system was modelled to determine basic features and to balance various factors that need to be optimized to maintain both functionalities (DMF-enabled droplet movement and RF detection) on the same chip. Simulated and experimental results show good agreement. Using a portable measurement setup, the integrated CSSR sensor was used to effectively identify a series of DMF-generated drops of ethanol–water mixtures of different compositions by measuring the resonant frequency of the CSSR. In addition, we show that a binary solvent system (ethanol/water mixtures) results in consistent changes in the measured spectrum in response to changes in concentration, indicating that the sensor can distinguish not only between pure solvents from each other, but also between mixtures of varied compositions. We anticipate that this system can be refined further to enable additional applications and detection modes for DMF systems and other portable sensing platforms alike. This proof-of-principle study demonstrates that the integrated DMF–CSSR sensor provides a new platform for monitoring and characterization of liquids with high sensitivity and low consumption of materials, and opens the way for new and exciting applications of RF sensing in microfluidics.

Received 8th May 2024,
Accepted 19th August 2024

DOI: 10.1039/d4lc00406j

rsc.li/loc

Introduction

Digital microfluidics (DMF) is a platform that enables manipulation of liquid drops without the need for enclosed channels, enabling a variety of droplet movement and manipulation techniques not possible using conventional microfluidic channels.[1,2] Through control of voltages applied to an array of actuation electrodes on a DMF chip, droplets are moved by dynamic control over spatially-confined, voltage-induced changes in wettability of adjacent electrodes. Because no channels are needed, experiments can be designed and reconfigured by simply programming the applied voltages, allowing automation of fluidic operations such as droplet dispensing, moving, splitting, merging, and mixing.[3] The programming aspect of DMF is a unique feature that enables automation with on-the-fly reconfigurability and versatility. DMF can be used to readily prepare a sample for off-chip detection, but fully integrated on-board detection provides significant advantages, especially for point-of-need measurements. To date, several integrated sensing modes have been demonstrated: nuclear magnetic resonance spectroscopy,[4,5] electrochemistry,[6–8] mass spectrometry,[9,10] chemiluminescence,[11] fluorescence,[12–14] surface plasmon resonance spectroscopy,[15] surface-enhanced Raman spectroscopy,[16] and colorimetry.[17,18]

Passive radio-frequency (RF) sensors present an attractive transduction technique for DMF-integrated measurements that quantify changes in dielectric or magnetic properties of a liquid under test (LUT). Ring resonators in particular have been widely used in various sensing applications, with the split-ring resonator (SRR, whereby split rings are made of a conductive material surrounded by dielectric) and complementary split-ring resonator (CSRR, whereby split rings are defined by removing portions of the metallic ground plane) being increasingly popular due to their small size, high sensitivity, low

[a] *Quantum and Nanotechnologies Research Centre, National Research Council Canada, Edmonton, AB T6G 2M9, Canada. E-mail: nikola.pekas@nrc-cnrc.gc.ca*
[b] *Department of Mechanical Engineering, University of Alberta, Edmonton, AB T6G 1H9, Canada*
[c] *Department of Chemistry, Queen's University, Kingston, ON, K7L 3N6, Canada*
[d] *Department of Chemistry, University of British Columbia - Okanagan Campus, Kelowna, BC, V1V 1V7, Canada*

† Electronic supplementary information (ESI) available. See DOI: https://doi.org/10.1039/d4lc00406j

cost, and simple design and fabrication. SRRs and CSRRs have been used as microwave sensing elements in applications including angular rotation detection,[19] 2D displacement sensing,[20] detection of wear particles in oil,[21] and permittivity characterization of crude samples.[22] Furthermore, SRRs and CSRRs have also seen applications in traditional channel-based microfluidics over the past decade, primarily for dielectric characterization of liquid materials. For instance, microwave sensing has been incorporated with channel microfluidics for multi-resonator detection of ethanol and KCl mixtures,[23] quantification of glucose blood levels,[24] detection of viruses using differential measurements,[25] characterization of protein structural unfolding,[26] decoupled sensing and microwave heating of liquid droplets,[27] and quality assessment of edible oils based on a change in dielectric constant after heating.[28]

In this paper, we add to prior work on incorporating microwave technology into DMF (for localized heating and dielectric sensing[29,30]) by demonstrating the integration of RF sensing elements (CSRRs) directly into a DMF chip. This is achieved by selective removal of the DMF ground-plane metallization to create CSRR structures that resonate at microwave frequencies and respond to changes in dielectric properties in their immediate surroundings. Sensing CSRRs are coupled to a transmission line patterned on the top side of the same substrate, enabling readout of changes in resonant behaviour using a vector network analyser (VNA). We then demonstrate reliable detection and differentiation of droplets composed of a variety of solvents, including binary mixtures, through measurements of reversible changes in the spectral shape and resonant frequencies in the 1–5 GHz range when droplets are moved over the sensor. Overall, this work shows a pathway to incorporate RF sensing into a range of experiments that expand the capabilities of DMF systems.

As a crucial proof-of-concept demonstration, we chose ethanol–water mixtures as a target analyte due to their relevance in the emerging field of microfluidic droplet-based platforms for optimization of biofuel production.[31] Efficient screening of various strains of microorganisms across varied fermentation conditions in microbioreactors requires integrated methods for monitoring the concentration of ethanol and other products.[32,33] We show that passive CSRR sensors can be fully integrated with DMF, and provide a promising and simple alternative to reagent-based bioassay methods. Digital microfluidics allows for on-chip compartmentalization and incubation of microorganisms inside droplets,[31] along with mixing and timed delivery of various formulations of growth media to droplet bioreactors. Finally, DMF enables controlled, real-time sampling of products that, as we demonstrate here, can be quantified by using microwave-resonant structures in the DMF ground electrode.

Device design and numerical simulations

Comprehensive reviews discussing DMF formats, fabrication, theories for droplet movement, and applications can be readily found in literature reports.[1,2] Briefly, DMF uses a fixed array of metal electrodes to realize droplet movement. The electrodes are typically patterned on a glass substrate, with a thin insulating layer deposited on top of the electrodes to prevent electrolysis of the liquid samples (applied voltages are usually within 80–110 V, depending on DMF structural composition[1]). To facilitate smooth movement of droplets, it is necessary to render the dielectric layer surface hydrophobic. To complete the electrical circuit, a ground electrode is also required.

Fig. 1(a) shows a schematic diagram of a typical dual-plate DMF system. The top plate electrode serves as the ground plane for the actuation electrodes that are patterned in the bottom plate. The gap between the plates defines the volume within which droplets are manipulated. For applications requiring droplet sensing, an external detector can be used (for example, a photomultiplier tube to collect light from a chemiluminescent reaction[34]), or a sensing mechanism can be integrated *via* modifications to the bottom or top DMF plate structures, usually in the form of electrochemical sensors.[35–37] These modifications often cause limitations to device versatility, droplet movement, or reusability. Here, we add localized sensing functionality by patterning the existing ground plane. Since patterns that constitute CSRR sensors are much narrower than the size of the DMF electrodes, our approach does not

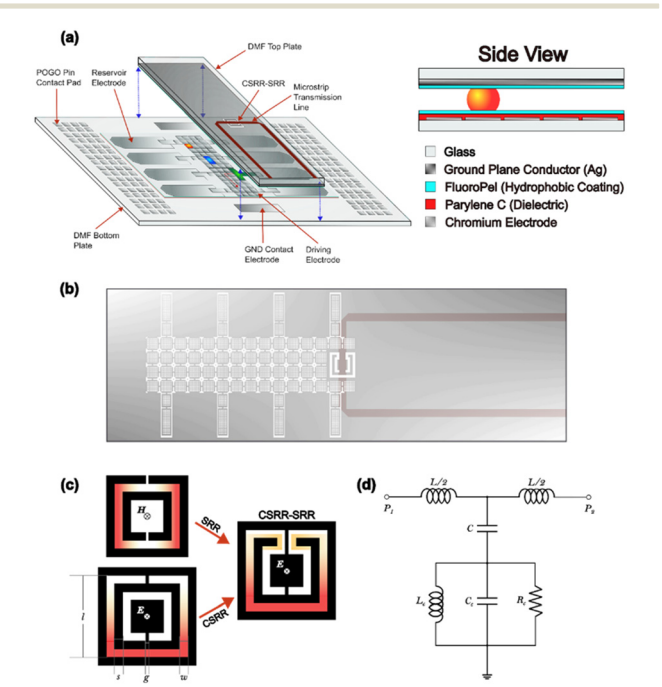

Fig. 1 (a) Schematic of the DMF system, showing the location of the droplet control electrodes relative to the microwave sensing element integrated into the top plate. (b) Top-down perspective view of the DMF top plate, with the CSRR–SRR and square features etched in white, and the copper transmission line stuck on the back side. (c) Modelled 2D electric field distributions, geometric parameters, and incident excitation fields associated with simple concentric SRR and CSRR geometries. Conductive features are shown in black. (d) Common RLC equivalent circuit model describing the behaviour of a resonating CSRR element.

interfere with the DMF operation. Fig. 1(b) shows the top plate design comprising the CSRR sensing region and the rest of the DMF ground plane in the form of a grid. Unlike solid metallic layers, the grid pattern allows for optical monitoring of droplets while maintaining the DMF and sensing functionalities. Fig. 1(b) also depicts a 50 Ω microstrip transmission line positioned on the substrate opposite side in relation to the ground plane. Fig. 1(c) and (d) show the CSRR geometric design and a typical CSRR resistor-inductor-capacitor (RLC) equivalent circuit, respectively, where w is the ring width of a ring resonator, s is the gap width between rings, g is the gap width of the slits, and l is the side length of the largest ring. The resonant frequency of a ring resonator is inversely proportional to the square root of its capacitance, which itself is dependent on the electric field distribution across the resonator. More intensive field build-up over a larger area leads to more significant changes in capacitance, and hence a greater shift in resonant frequency when the surrounding dielectric properties change; this shift is the primary sensing principle governing many RF sensors. Here, we refer to one of the sensing structures as CSRR–SRR because it consists of a CSRR structure containing an internal metallic ring, which confers resonant properties akin to SRR structures.

We refer to theoretical simulations and empirical results in the case of sensors fabricated in the DMF ground plane and assembled with the DMF bottom plate as on-DMF, while off-DMF refers to sensors fabricated in the identical ground plane, but used without being mounted onto the bottom plate of the DMF device.

Finite-element electromagnetic simulations were performed in Ansys HFSS to understand the resonance behaviour of the CSRR–SRR structure, shown in Fig. 2(a). The supporting glass substrate (pink) was assumed to be soda-lime glass with a dielectric constant of 7.2 and loss tangent of 0.007 at 1 MHz, based on values found from the manufacturer.[38] This was modelled as a 1 mm thick 3D block, and frequency-dependency of dielectric constant and loss tangent were accounted for by implementing a Djordjevic–Sarkar model.[39] A 1.3 mm wide Cu microstrip transmission line (green) was positioned atop the glass substrate and extruded by 35 μm, with two planar rectangles modelled at the ends of the TL for simulating electrical ports to the VNA. To simulate the power provided by the VNA along with the 50 Ω matched SMA connectors, lumped port boundary conditions were applied to these rectangular faces. The CSRR–SRR structure itself (purple-coloured regions, signifying removed portions of the ground plane metal) was developed as a 2D object and extruded to become a 1 μm thick block of silver metal, which was assigned to be ground from the perspective of the lumped ports. With limited information, the FluoroPel 1101 V layer was modelled as a 160 nm 3D object with a dielectric constant and loss tangent of 1.9 and 0.0007 respectively, at 0.1 GHz. The dielectric constant was provided on the Cytonix website, and the loss tangent was estimated based on specifications provided by a different manufacturer of fluoropolymers.[40] Finally, to simulate off-DMF conditions with liquid analyte, a 50 μL LUT droplet was modelled as a cut-out of a sphere. For a water droplet, the radius was 3 mm to just enclose the CSRR–SRR structure; for organic solvents the radius was increased to 3.75 mm which was offset by cutting out more of the sphere. This ensured more accurate approximation of the observed wetting properties of these droplets. Of note, an auto-open region was assigned to enclose the simulation space.

The geometrical parameters of dielectric width (w), metal width (s), and the split ring gap width (g), illustrated in Fig. 1(c), were chosen to be 0.35, 0.2, and 0.6 mm respectively, as determined by an Optimetrics parameter sweep, yielding optimal resonance at approximately 4 GHz. As seen in Fig. 2(b), the simulated CSRR–SRR structure in air resonates slightly above 4 GHz, while measured result has a slightly lower peak magnitude and is shifted slightly to 4.2 GHz. Furthermore, the inset of Fig. 2(b) shows that the CSRR–SRR does indeed show a hybrid blend of electric field distributions characteristic of a CSRR and SRR individually, which improves the response of the structure for the expected droplet sizes: due to the broader electric field distribution, more of the droplet's dielectric nature is seen by the CSRR–SRR structure, leading to greater sensitivity. A comparison of the resonant behaviour between a CSRR–SRR and CSRR of the same dimensions can be seen in Fig. S1.†

Deionized water (DI), acetone, isopropyl alcohol (IPA), and ethanol (EtOH) were modelled as materials in HFSS, using interpolation of published results[41] to determine the dielectric constant and loss tangents of these LUTs at specific frequencies. A 50 μL droplet was modelled (Fig. 2(a)) for each analyte separately, and the simulation results can be seen in Fig. 2(c). LUTs with larger permittivity tend to shift the resonant frequency to lower values, while also attenuating the transmission coefficient. Loss tangent also plays a significant role as evidenced by the spectra for EtOH, which is known to

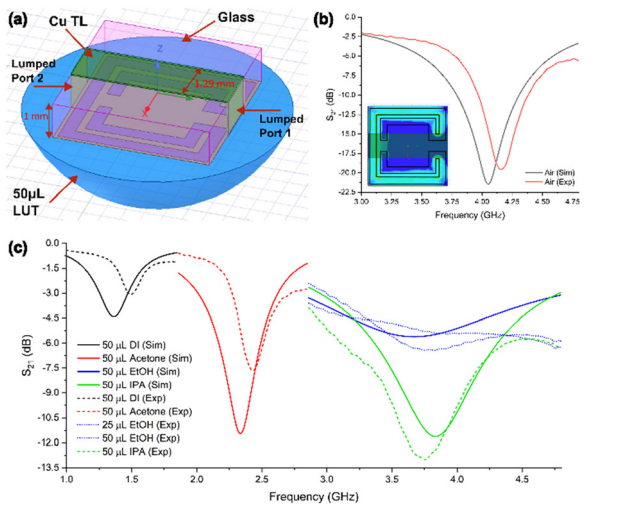

Fig. 2 (a) Setup of the CSRR–SRR unit cell in Ansys HFSS for microwave simulations. (b) Comparison of simulated (black) transmission response in air to the experimental result (red). The inset shows the simulated electric field distribution at 4 GHz. (c) Comparison of simulated (solid) and experimental (dashed) transmission responses for LUT droplets drop-casted onto the CSRR–SRR structure, outside of DMF.

broaden the resonance peak.[42] Generally, the simulation and experimental spectra tend to agree, although more rigorous modelling of and more advanced fabrication techniques would be necessary for accurate quantitative analysis and further design optimization. Our results indicate that the analytes considered here are expected to cause readily measurable changes in resonant properties, demonstrating that integrated microwave sensing can distinguish between different liquids in DMF devices.

To integrate the ground-plane microwave resonant structures as sensors into a fully functional DMF device, we must consider the requirements and the limitations posed by both aspects of the overall system. It is desirable to have droplets visible, at least at the early research and development phase, to allow for droplet tracking during dispensing, delivery to the sensing regions, and droplet removal. It should also be noted that the thickness of the structured ground-plane conductor affects the wetting behaviour and movement of droplets over topographic features. The choice of ground plane material is therefore paramount to realize both DMF and sensing capabilities, as one must take into consideration the conductivity, skin effect depth, thickness, and the optical transparency of the ground-plane conductor. Generally, ultra-thin metal films and conductive transparent oxides, such as the indium tin oxide (ITO) layer used to provide optical access in conventional DMF top plates, cannot be used due to relatively high resistivity and consequently high losses at the microwave frequencies. For DMF experimentation, a ~160 nm thick layer of 10 Ω sq^{-1} ITO is typically used for the top plate. Using online skin depth calculators,[43,44] it can be determined that the skin depth for 10 Ω sq^{-1} ITO is ~10 μm at 4 GHz, which is far too thick a layer for practical physical vapour deposition techniques. Through finite-element electromagnetic simulations in Ansys HFSS, we have compared resonant profiles from ITO and Cu ground planes for varying thicknesses (Fig. S2†), validating the need for ground planes of skin depth thickness to achieve acceptable resonance. In recent years, researchers have demonstrated that SRRs and CSRRs can be fabricated in relatively thin films of thicknesses on the order of, or somewhat smaller than, the skin depths of the metals of interest, such as Ag and Au, at the desired frequencies.[45,46] Thus, owing to its high conductivity, relatively low cost, and clean deposition compared to Cu, we chose to use Ag as the ground plane material in the proof-of-principle devices presented here, which produces an ample resonant signal when deposition thickness is on the order of 1 μm.

Materials, methods, and fabrication

For DMF experimentation, DropBot hardware (model D83-120) was purchased from Sci Bots Inc. (Toronto, ON, Canada) and interfaced with associated open source MicroDrop software version 2.3 for droplet actuation; pre-made DropBot chips with chromium driving electrodes were also purchased from Sci-Bots Inc. and were used for the DMF bottom plate. One millimetre thick, 25 mm by 75 mm microscope glass slides were purchased from Fisher Scientific (12-544-4, Ottawa, ON, Canada) and were used for DMF top plate fabrication. To attach the DMF bottom and top plates together, double sided conductive tape (1-5-9719) was purchased from DigiKey (Thief River Falls, MN, USA). FluoroPel 1101 V (1% fluoropolymer in fluorosolvent) was purchased from Cytonix (Beltsville, MD, USA), and all other chemicals, such as liquids under test and Au etchant, were purchased from Sigma Aldrich (Oakville, ON, Canada), unless otherwise specified.

For microwave sensing, a TR5048 two port 4.8 GHz vector network analyzer (VNA) from Copper Mountain Technologies (Indianapolis, IN, USA) was used, in conjunction with 50 Ω coaxial cables. Coaxial SMA connectors from Linx Technologies (CONSMA020.042-G, Boynton Beach, FL, USA) were soldered to the microstrip transmission line (TL) using lead-free solder and connected to the coaxial cables to enable microwave measurements. For reading VNA spectra, associated TRVNA 23.1.2 software was used. The TL was rapidly prototyped by cutting a copper shielding tape 1181 RF EMI (3 M, Maplewood, MN, USA), with copper thickness of 36 μm and additional 30 μm thick conductive acrylic adhesive. The TL was either cut with a surgical blade by hand, or using a vinyl cutter (Cricut Maker, South Jordan, UT, USA), and temporary transfer tape was used to align and adhere the cut TL to the DMF top plate.

Ground plane fabrication

The CSRR–SRRs were patterned on the silver DMF ground plane of the glass top plate as follows. First, glass substrates were cleaned with a 10 minute acetone bath with slight agitation, followed by quick rinses with IPA and DI water, and drying with nitrogen. After cleaning, substrates were loaded into a Johnsen Ultravac electron beam evaporation system (model 98-016, Burlington ON, Canada) for deposition of 5 nm of the adhesion interlayer Ti at 0.5 Å s^{-1}, followed by a 1100 nm Ag deposition at 3 Å s^{-1}. The Ag layer thickness is on the order of one skin depth at ~4.5 GHz. After deposition, substrates were stored in nitrogen to avoid oxidation of silver prior to metal patterning. A standard photolithographic process was used to pattern the CSRR–SRR structures, as well as the DMF ground plane grid pattern. To increase photoresist adhesion, substrates were first treated with hexamethyldisilazane (HMDS) for 20 min in a vapour prime oven (Yield Engineering systems, Fremont, CA, USA). Then, AZ 1529 positive-toned photoresist (EMD Performance Materials Cop., Philadelphia, PA, USA) was spin-coated onto the substrates at 500/3000 RPM spread/spin for 10/60 s, followed by baking at 100 °C for 60 s to yield a photoresist layer ~3.4 μm thick. This ensured that we had a thick enough layer to appropriately etch Ag and Ti using wet and plasma etching, respectively. UV exposure was subsequently done with a MLA150 maskless aligner (Heidelberg Instruments, Heidelberg, Baden-Württemberg, Germany) at 350 mJ cm^{-2} on fast mode with a custom mask pattern designed in KLayout. Photoresist was developed in AZ 400 K 1:4 developer (AZ Electronic Materials, Wiesbaden, Hesse, Germany) for 120 s, followed by DI rinsing and N_2 drying. Without removing the photoresist

layer, Ag was wet etched using a KI:I2 etchant (651818, Sigma) for 2 minutes at room temperature, with a subsequent DI rinse and N_2 dry. Next, the 5 nm Ti adhesion layer was dry-etched for 15 s at 20 °C using a PlasmaPro 100 Cobra system (Oxford Instruments, Ottawa, ON, Canada), with a fluorine-based etch recipe containing 15 sccm SF_6, 15 sccm CHF_3, and 10 sccm Ar. Crystalbond 555HMP adhesive (SPI Supplies, West Chester, PA, USA) was used to mount the glass substrates on 4″ Si wafers carriers for the dry-etching process. After plasma etching of Ti was completed, Crystalbond adhesive was removed with DI water, and the remaining photoresist was stripped with acetone, followed with an IPA and DI rinse.

Finally, FluoroPel 1101 V was spin-coated onto the patterned substrates at 2000 RPM for 30 s, and then baked at 150 °C for 20 min to enable DMF droplet movement and to prevent oxidation of silver. Prior to spin-coating of FluoroPel, the portion of the ground plane where the SMA connectors were to be soldered was protected using dicing tape (18733, Semiconductor Equipment Corp, Moorpark, CA, USA). The complete fabricated DMF top plate can be seen in Fig. 3(a).

DMF microwave sensing setup

The DMF top-plate was mounted to the DMF bottom-plate using a double layer of double-sided conductive tape, resulting in the gap between the plates of ~180 μm. This configuration ensures that each DMF driving electrode can hold approximately 1 μL of liquid. After assembly, the DMF device was loaded into a custom device holder and connected to DropBot instrument using an extension module, as seen in Fig. 3(c). The custom holder apparatus was designed in TinkerCAD (Autodesk, San Francisco, CA, USA), sliced using the Ultimaker Cura software (Ultimaker, Brooklyn, NY, USA) and 3D printed using polylactic acid filaments in a Rostockmax v4 Delta Printer (SeeMeCNC, Ligonier, IN, USA), to allow for enough room to connect SMA connectors and coaxial cables. The DMF device was positioned parallel to the bench surface such that the coaxial cables could lay flat on the bench, avoiding strain that could damage the connectors and the cables, and lead to signal variations (Fig. 3(d)). Liquid under test solutions were pipetted onto the DMF reservoirs (5 μL), and droplet dispensing and movement was controlled *via* Microdrop software (Sci-Bots) *via* automated protocol and monitored in real time using a camera mounted over the device (LifeCam Studio, Microsoft, Redmond, WA, USA).

To prepare the VNA for measurements, the VNA was first calibrated off-DMF for S_{21} measurements with a standard through connector. The IF bandwidth was set to 10 kHz, and averaging (with the factor of 10) and smoothing (with the aperture of 3%) were enabled. Furthermore, 2001 data points between 20 kHz and 4.8 GHz were collected.

Preparation and measurement of liquid samples

Water–ethanol solutions were prepared in different concentrations prior to measurements. First, stock DI water and ethanol (EtOH) solutions were prepared with 5% 90R4 surfactant in a 98 : 2 ratio by volume. Using these stock solutions, 20%, 40%, 60%, and 80% DI–EtOH mixtures were prepared. For all measurements, 5 μL of a sample was injected into the desired DMF reservoir. The volume of sample droplets was chosen to ensure full droplet coverage over the sensing region for maximal sensitivity in the resonant frequency shift. As can be seen in Fig. S3,† this shift becomes less pronounced when droplet footprint becomes smaller than the size of the sensing region. After measurements, liquid in the collection reservoir was wicked away with Kimwipe tissue. When the droplet was delivered by DMF action to the CSRR–SRR sensing area, the S_{21} signal was given 5–10 s to stabilize, after which it was saved. This process was repeated for all samples.

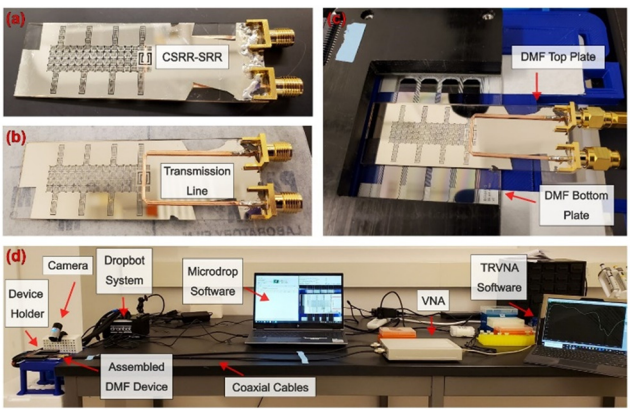

Fig. 3 Apparatus for CSRR–SRR integrated with DMF. (a) Top plate view highlighting the CSRR–SRR structure and ground grid on silver DMF ground plane. (b) Back view of top plate, showing the positioning of the copper microstrip transmission line. (c) Assembled DMF device mounted on custom holder for DMF control system. (d) Full apparatus overview, showing all necessary software and hardware for enabling microwave measurements with droplet movement.

Results and discussion

Fig. 3(a) and (b) show the Ag plane and transmission line top-down views of the fabricated DMF top-plate glass substrate, showing the DMF ground grid and SMA connector positions. Fig. 3(c) shows a fully assembled device mounted on the DMF control systems (DropBot) using an extension module and a custom-made chip holder. Fig. 3(d) shows a representation of the full apparatus, including DMF system, computer, VNA, coaxial cables, device holder, and camera.

Due to the non-transparent nature of Ag, we have designed a ground grid with 160 μm × 160 μm openings to allow for droplet visualisation. DMF droplet movement using a fabricated top plate with ground grid is demonstrated in Video S1.† When probing droplet movement with a 10 mM PBS solution supplemented with 0.1% Tetronic 90R4 on the assembled DMF device, an average velocity of 4.6 ± 1.0 mm s^{-1} was obtained (estimated from video data), indicating average velocities that are comparable with other reported DMF systems.[47,48] The droplet can be easily delivered to, and removed from the sensing structure regions using an automated protocol. Droplet

splitting was also possible with this design, but it required longer electrode actuation transitions (3–4 s) in comparison to regular ITO top plates (1–1.5 s). Thus, the system demonstrates adequate DMF performance for the proof-of-concept integration discussed herein.

Initial investigations concerning the effect of DMF integration on the measured microwave signal (resonant frequency and peak attenuation) were performed for two sets of CSRR–SRR dimensions (Fig. 4). Of note, two resonant frequencies were observed: one higher resonant frequency attributed to the resonance of the CSRR–SRR, and the lower resonant frequency attributed to the etched squares immediately surrounding the CSRR–SRR (Fig. 1(b)). For a ring thickness w = 0.4 mm, a ring gap width s = 0.4 mm, and a split-ring gap width of g = 1.0 mm, the CSRR–SRR resonant behaviour in air both on- and off-DMF can be seen in Fig. 4(a). A clear redshift in the off-DMF resonant frequencies of ~4.5 GHz (CSRR–SRR) and ~3.85 GHz (etched squares) is observed upon mounting the top plate containing the sensor onto the DMF bottom plate, which is indicative of the presence of the capacitance of the bottom plate. This shift is most pronounced for the CSRR–SRR peak, which redshifts by approximately 500 MHz to 4 GHz. Further evidence linking the effect to the bottom plate is the significant decrease in the S_{21} peak attenuation for both resonant frequencies. These effects also present themselves in air for a CSRR–SRR with dimensions w–s–g = 0.35–0.2–0.6 mm, as seen in Fig. 4(b). The CSRR–SRR resonates at around 4.13 GHz off-DMF, with the etched squares resonating around 3.85 GHz as expected. Upon mounting the sensor above the DMF bottom plate, both resonant frequencies shift to the same position of ~3.63 GHz and hence overlap. Exactly like the 0.4–0.4–1.0 mm CSRR–SRR, the resonant frequency of is redshifted by around 0.5 GHz. This consistency provides further evidence that the bottom plate is the cause of the drastic frequency shift and peak attenuation upon assembling the complete device.

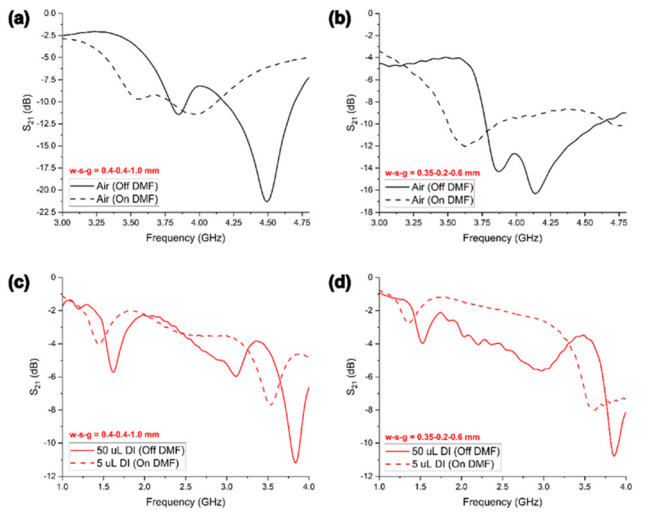

Fig. 4 CSRR–SRR resonant peaks on- and off-DMF device using two different sensor architecture dimensions. w–s–g were 0.4–0.4–1.0 mm (a and c) and 0.35–0.2–0.6 mm (b and d). Measurements done in air (a and b) and DI water (c and d).

For studying the viability of the resonating CSRR–SRR as a sensing element, the response to deionized water was evaluated on- and off-DMF. For off-DMF measurements, 50 μL droplets of DI water were pipetted onto the resonator. For on-DMF measurements, 5 μL droplets of DI water (supplemented with 0.1% 90R4) were dispensed to the DMF sensor region from the reservoir using DMF droplet actuation. Both volumes ensured coverage of the entire CSRR–SRR region, akin to that shown in Fig. 2(a). For the CSRR–SRR with dimensions 0.4–0.4–1.0 mm in Fig. 4(c), the etched-square resonant frequency on DMF remains fixed at approximately 3.55 GHz (as seen and discussed for Fig. 4(a)), whereas the CSRR–SRR resonant frequency redshifted to near 1.4 GHz with a significant drop in peak attenuation. This drastic redshift was also observed off-DMF for a 50 μL DI droplet, with a sharper peak compared to the droplet on DMF, as expected. This behaviour was also prominent for a CSRR–SRR with dimensions 0.35–0.2–0.6 mm as seen in Fig. 4(d), where the on-DMF etched square resonant frequency remained fixed and the CSRR–SRR resonant frequency experienced significant redshift and peak attenuation loss in the presence of DI water (both on- and off-DMF). While the former set of geometrical dimensions (0.4–0.4–1.0 mm) evidently provided greater peak attenuations compared to the latter set of dimensions, the latter set provided smoother curves over the frequency range of interest (1 to 3 GHz). Therefore, a CSRR–SRR with dimensions 0.35–0.2–0.6 mm was used for further sensing evaluation.

For qualitative and quantitative microwave sensor performance evaluation, the binary mixture of water and ethanol in varying volume fractions can be used.[49] This was adopted in the present work, with the addition of 0.1% 90R4 surfactant in each binary mixture for ease of droplet dispensing and movement with DMF. The water volume fraction was changed from 100% to 0%, in steps of 20%. At each step, this measurement was done three times with three new sample droplets. The averages of these spectra were then taken for each step, with the final plot presented in Fig. 5(a). The raw S_{21} spectra for both sets of CSRR–SRR dimensions are shown in Fig. S4 and S5.† Furthermore, Fig. 5(b) shows a plot of resonant frequency and peak amplitude trends as a function of DI water fraction observed in the integrated readings. Based on the resonant frequency shift alone, concentration of ethanol can be determined with relatively high sensitivity in the high-concentration range (low water fraction), while at the lower concentration range (high water fraction) the sensitivity is somewhat diminished. If two linear regions are established below and above the 40% water fraction, the sensitivity for the highly concentrated ethanol region is 17.2 MHz/% EtOH, while the sensitivity for the low concentrated ethanol region is 4.4 MHz/% EtOH. However, the S_{21} peak intensity data provides high sensitivity in the low-concentration range, enabling composition analysis across the full range of concentrations with sensitivity comparable to or better than the microwave

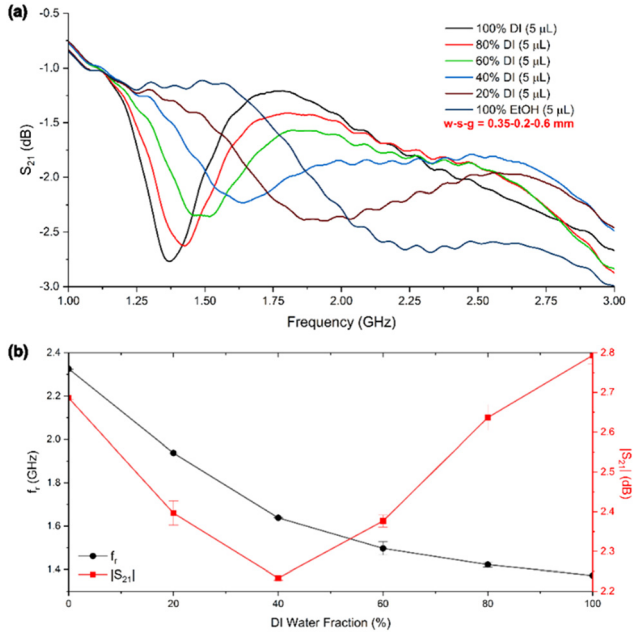

Fig. 5 DMF-integrated CSRR–SRR for detection of water–ethanol mixtures (a) S_{21} spectra showing the average resonant profile for each tested condition; (b) trends in resonant frequency f_r and S_{21} peak intensity as a function of DI water fraction.

sensing[50] and colorimetric bioassays[32] in similar microfluidic environments. In contrast to the work presented by Ebrahimi *et al.*,[49] the present CSRR–SRR exhibits a slightly nonlinear response in resonant frequency shift, but with relatively small standard deviations shown as error bars in Fig. 5(b). The same non-linear behaviour was also observed on sensors designed with different *w*–*s*–*g* dimensions (Fig. S5†), suggesting that the behaviour is not due to systematic errors but that it could be an effect of the novel geometry used here. Further investigation would be required to understand this phenomenon, which is beyond of the scope of present work and may be pursued in the future. The quadratic behaviour of the peak attenuation, however, is comparable to that from ref. 49, where a minimum is observed at 40% water fraction. The system demonstrated remarkable recovery ability once the sample droplet was moved away from the sensing region, with restoration of the air signal profile (Fig. S6,† resonant peak at 3.633 ± 0.004 GHz, intensity −10.4 ± 0.7 dB). Therefore, the CSRR–SRR on-DMF provides high versatility with the ability to be used as a high-sensitivity frequency-based sensor, or an amplitude-based sensor, depending on the need. The integration with DMF is especially important for potential applications where off-chip handling of samples can pose serious challenges.

Conclusions and future work

We have demonstrated on-chip sensing of droplets in a DMF device by structuring the DMF ground plane to create microwave-frequency resonant regions that serve as passive sensors. The presence or absence of the droplet, and makeup of the droplet, result in reproducible changes in resonant properties of the sensor, which are easily observed by coupling the sensor to a microstrip line, and measuring the power transmission spectrum of the microstrip line, S_{21}. We have also demonstrated that the sensor empirical performance is in agreement with simulated data for solvents spanning a wide range or permittivity constants (from ~3.2 for IPA to ~77.5 for DI). The sensor response on the integrated device was also quite reproducible, with complete regeneration of air signal upon removal of droplets. Since sensing region is well confined within the footprint of the CSRR structure (Fig. 1(b)), it should be possible to sequentially read signals of multiple droplets as they are moved through the sensing region, and to include an array of independent sensors on a single DMF chip for scalable multiplexed sensing.

While proof-of-concept devices presented in this manuscript were fabricated in-house using silver as the ground plane metal, we are also working on deploying standard copper microwave circuitry. To this end, planarization of the dielectric layer will be required to avoid disruption of the DMF functionality due to topographic features in the ground plane, as copper thickness in commercial microwave printed-circuit boards is typically tens of micrometres.

It should be noted that, in principle, split-ring resonators will respond not only to changes in dielectric properties of the immediate environment, but also to changes in magnetic permeability. Magnetic nanoparticles or micrometre-sized magnetic beads could therefore be used as reporters in DMF systems, while at the same time creating interesting opportunities for interplay between magnetic and electrowetting forces for sample manipulation and for analytical separations. Overall, we anticipate that the integration of microwave sensing with DMF will lead to creative applications that benefit from both technical simplicity and cost-effectiveness such that such measurements can be done using inexpensive and portable VNAs.

Data availability

The data supporting this article have been included as part of the ESI.†

Author contributions

Dipesh Aggarwal: experimental design, device fabrication, data collection and analysis, and writing. Richard Piffer Soares de Campos: experimental design, device fabrication, data collection and analysis, writing. Abebaw B. Jemere: consulting on experimental design, data analysis, writing. Adam Johan Bergren: consulting on experimental design, data analysis, writing. Nikola Pekas: overall concept and experimental design, device fabrication, data collection and analysis, writing.

Conflicts of interest

There are no conflicts to declare by any of the authors.

Acknowledgements

The authors would like to first acknowledge the contribution of the nanoFAB, situated at the University of Alberta, with regards to photolithographic equipment used and expertise provided by Tim Harrison and Gustavo de Oliveira Luiz to guide this project. We would further like to acknowledge and thank John Canlas and Tim Patrie from the Quantum and Nanotechnologies Research Centre, National Research Council Canada, for their advice and training help in relation to electron-beam evaporation. Finally, we also acknowledge the contribution of Dr Mehdi Nosrati for fruitful discussion in the early stages of the work.

Notes and references

1 M. Abdelgawad and A. R. Wheeler, The Digital Revolution: A New Paradigm for Microfluidics, *Adv. Mater.*, 2009, **21**(8), 920–2925.
2 K. Choi, A. H. C. Ng, R. Fobel and A. R. Wheeler, Digital Microfluidics, *Annu. Rev. Anal. Chem.*, 2012, **5**, 413–440.
3 R. Fobel, C. Fobel and A. R. Wheeler, DropBot: An open-source digital microfluidic control system with precise control of electrostatic driving force and instantaneous drop velocity measurement, *Appl. Phys. Lett.*, 2013, **102**, 193513.
4 B. Wu, S. von der Ecken, I. Swyer, C. Li, A. Jenne and F. Vincent, *et al.*, Rapid Chemical Reaction Monitoring by Digital Microfluidics-NMR: Proof of Principle Towards an Automated Synthetic Discovery Platform, *Angew. Chem., Int. Ed.*, 2019, **58**(43), 15372–15376.
5 I. Swyer, S. von der Ecken, B. Wu, A. Jenne, R. Soong and F. Vincent, *et al.*, Digital microfluidics and nuclear magnetic resonance spectroscopy for in situ diffusion measurements and reaction monitoring, *Lab Chip*, 2019, **19**(4), 641–653.
6 Y. Zhang and Y. Liu, A Digital Microfluidic Device Integrated with Electrochemical Impedance Spectroscopy for Cell-Based Immunoassay, *Biosensors*, 2022, **12**(5), 330.
7 N. Ruecha, J. Lee, H. Chae, H. Cheong, V. Soum and P. Preechakasedkit, *et al.*, Paper-Based Digital Microfluidic Chip for Multiple Electrochemical Assay Operated by a Wireless Portable Control System, *Adv. Mater. Technol.*, 2017, **2**(3), 1600267.
8 R. P. S. de Campos, D. Aggarwal, N. W. C. Chan and A. B. Jemere, An integrated digital microfluidic electrochemical impedimetric lipopolysaccharide sensor based on toll-like receptor-4 protein, *Biosens. Bioelectron.: X*, 2024, **16**, 100433.
9 A. Das, C. Weise, M. Polack, R. D. Urban, B. Krafft and S. Hasan, *et al.*, On-the-Fly Mass Spectrometry in Digital Microfluidics Enabled by a Microspray Hole: Toward Multidimensional Reaction Monitoring in Automated Synthesis Platforms, *J. Am. Chem. Soc.*, 2022, **144**(23), 10353–10360.
10 Q. Ruan, J. Yang, F. Zou, X. Chen, Q. Zhang and K. Zhao, *et al.*, Single-Cell Digital Microfluidic Mass Spectrometry Platform for Efficient and Multiplex Genotyping of Circulating Tumor Cells, *Anal. Chem.*, 2022, **94**(2), 1108–1117.
11 K. Jin, C. Hu, S. Hu, C. Hu, J. Li and H. Ma, "One-to-three" droplet generation in digital microfluidics for parallel chemiluminescence immunoassays, *Lab Chip*, 2021, **21**(15), 2892–2900.
12 J. Shen, L. Zhang, J. Yuan, Y. Zhu, H. Cheng and Y. Zeng, *et al.*, Digital Microfluidic Thermal Control Chip-Based Multichannel Immunosensor for Noninvasively Detecting Acute Myocardial Infarction, *Anal. Chem.*, 2021, **93**(45), 15033–15041.
13 H. Li, X. Liu, F. Zhu, D. Ma, C. Miao and H. Su, *et al.*, Spatial barcoding-enabled highly multiplexed immunoassay with digital microfluidics, *Biosens. Bioelectron.*, 2022, **215**, 114557.
14 R. Eswar, C. H. Brodie and C. M. Collier, Lock-In Amplified Fluorescence Spectroscopy in a Digital Microfluidic Configuration for Antibiotic Detection of Ciprofloxacin in Milk, *J. Microelectromech. Syst.*, 2022, **31**(6), 927–934.
15 L. Malic, T. Veres and M. Tabrizian, Nanostructured digital microfluidics for enhanced surface plasmon resonance imaging, *Biosens. Bioelectron.*, 2011, **26**(5), 2053–2059.
16 Y. Wang, Q. Ruan, Z.-C. Lei, S.-C. Lin, Z. Zhu and L. Zhou, *et al.*, Highly Sensitive and Automated Surface Enhanced Raman Scattering-based Immunoassay for H5N1 Detection with Digital Microfluidics, *Anal. Chem.*, 2018, **90**(8), 5224–5231.
17 Z. Gu, J.-J. Luo, L.-W. Ding, B.-Y. Yan, J.-L. Zhou and J.-G. Wang, *et al.*, Colorimetric Sensing with Gold Nanoparticles on Electrowetting-Based Digital Microfluidics, *Micromachines*, 2021, **12**(11), 1423.
18 P. Kanitthamniyom, P. Y. Hon, A. Zhou, M. Y. Abdad, Z. Y. Leow and N. B. M. Yazid, *et al.*, A 3D-printed magnetic digital microfluidic diagnostic platform for rapid colorimetric sensing of carbapenemase-producing Enterobacteriaceae, *Microsyst. Nanoeng.*, 2021, **7**(1), 47.
19 S. H. Zainud-Deen, H. A. Malhat and E. A. El-Refaay, A Rotational Planar Circular Split Ring Resonator Sensor for Angle Rotation Detection Applications, *Wirel. Pers. Commun.*, 2022, **124**(3), 2579–2591.
20 K. Ren, P. Zhu, T. Sun, J. Wang, D. Wang and J. Liu, *et al.*, A Complementary Split-Ring Resonator (CSRR)-Based 2D Displacement Sensor, *Symmetry*, 2022, **14**(6), 1116.
21 E. L. Chuma, Y. Iano, L. L. B. Roger, G. G. Oliveira and G. C. Vaz, Novelty Sensor for Detection of Wear Particles in Oil Using Integrated Microwave Metamaterial Resonators With Neodymium Magnets, *IEEE Sens. J.*, 2022, **22**(11), 10508–10514.
22 A. Rivera-Lavado, A. García-Lampérez, M.-E. Jara-Galán, E. Gallo-Valverde, P. Sanz and D. Segovia-Vargas, Low-Cost Electromagnetic Split-Ring Resonator Sensor System for the Petroleum Industry, *Sensors*, 2022, **22**(9), 3345.
23 K. Gao, J. K. Wu, X. Wang, N. Y. Kim, X. F. Gu and J. G. Liang, Specific Detection of Organic and Inorganic Solution Based on Microwave Resonator Array, *IEEE Sens. J.*, 2022, **22**(11), 10532–10540.
24 M. Zhang, X. Yang, M. Ren, S. Mao, R. Dhakal and N.-Y. Kim, *et al.*, Microfluidic microwave biosensor based on biomimetic materials for the quantitative detection of glucose, *Sci. Rep.*, 2022, **12**(1), 15961.

25 W. Cui, P. Zhao, J. Wang, N. Qin, E. A. Ho and C. L. Ren, Reagent free detection of SARS-CoV-2 using an antibody-based microwave sensor in a microfluidic platform, *Lab Chip*, 2022, **22**(12), 2307–2314.

26 J. Muñoz-Enano, O. Peytral-Rieu, P. Vélez, D. Dubuc, K. Grenier and F. Martín, Characterization of the Denaturation of Bovine Serum Albumin (BSA) Protein by Means of a Differential-Mode Microwave Microfluidic Sensor Based on Slot Resonators, *IEEE Sens. J.*, 2022, **22**(14), 14075–14083.

27 W. Cui, Z. Abbasi and C. L. Ren, Crosstalk analysis and optimization in a compact microwave-microfluidic device towards simultaneous sensing and heating of individual droplets, *J. Micromech. Microeng.*, 2022, **32**(9), 095005.

28 X. Han, Y. Zhou, X. Li, Z. Ma, L. Qiao and C. Fu, *et al.*, Microfluidic Microwave Sensor Loaded with Star-Slotted Patch for Edible Oil Quality Inspection, *Sensors*, 2022, **22**(17), 6410.

29 T. Markovic, S. Liu, I. Ocket and B. K. J. C. Nauwelaers, A 20 GHz microwave heater for digital microfluidic, *Int. J. Microw. Wirel. Technol.*, 2017, **9**(8), 1591–1596.

30 *Microwave Dielectric Sensing for Sample Preparation in Digital Microfluidics, 2019 14th International Conference on Advanced Technologies, Systems and Services in Telecommunications (TELSIKS)*, ed. Markovic T., Bao J., Maenhout G., Barmuta P., Schreurs D. and Ocket I., *et al.*, 23–25 Oct. 2019.

31 S. H. Au, S. C. C. Shih and A. R. Wheeler, Integrated microbioreactor for culture and analysis of bacteria, algae and yeast, *Biomed. Microdevices*, 2011, **13**(1), 41–50.

32 K. Churski, A. Ruszczak, S. Jakiela and P. Garstecki, Droplet Microfluidic Technique for the Study of Fermentation, *Micromachines*, 2015, **6**(10), 1514–1525.

33 S. Abalde-Cela, A. Gould, X. Liu, E. Kazamia, A. G. Smith and C. Abell, High-throughput detection of ethanol-producing cyanobacteria in a microdroplet platform, *J. R. Soc., Interface*, 2015, **12**(106), 20150216.

34 A. K. Knipes, A. Summers, A. A. Sklavounos, J. Lamanna, R. P. S. de Campos and T. Narahari, *et al.*, Use of a rapid digital microfluidics-powered immunoassay for assessing measles and rubella infection and immunity in outbreak settings in the Democratic Republic of the Congo, *PLoS One*, 2022, **17**(12), e0278749.

35 M. D. M. Dryden, D. D. G. Rackus, M. H. Shamsi and A. R. Wheeler, Integrated Digital Microfluidic Platform for Voltammetric Analysis, *Anal. Chem.*, 2013, **85**(18), 8809–8816.

36 D. G. Rackus, M. D. M. Dryden, J. Lamanna, A. Zaragoza, B. Lam and S. O. Kelley, *et al.*, A digital microfluidic device with integrated nanostructured microelectrodes for electrochemical immunoassays, *Lab Chip*, 2015, **15**(18), 3776–3784.

37 M. H. Shamsi, K. Choi, A. H. C. Ng and A. R. Wheeler, A digital microfluidic electrochemical immunoassay, *Lab Chip*, 2014, **14**(3), 547–554.

38 S. A. VIDRASA VeTyV, *Sodalime 9.1 Glass - Physical and Chemical Properties*, VIDRASA, Vidrio en Tubo y Varilla, S.A., 2024 [available from: **https://www.vidrasa.com/eng/products/arglas/arglas_pf.html**.

39 A. R. Djordjevic, R. M. Biljie, V. D. Likar-Smiljanic and T. K. Sarkar, Wideband frequency-domain characterization of FR-4 and time-domain causality, *IEEE Trans. Electromagn. Compat.*, 2001, **43**(4), 662–667.

40 *DAIKIN INDUSTRIES L. Electrical properties | Fluorochemicals*, 2024 [available from: **https://www.daikinchemicals.com/solutions/technical-challenges/electrical-properties.html**.

41 A. Y. Zarubina, S. G. Kibets, A. A. Politiko, V. N. Semenenko, K. M. Baskov and V. A. Chistyaev, Complex permittivity of organic solvents at microwave frequencies, *IOP Conf. Ser.: Mater. Sci. Eng.*, 2020, **862**(6), 062085.

42 A. Salim and S. Lim, Complementary Split-Ring Resonator-Loaded Microfluidic Ethanol Chemical Sensor, *Sensors*, 2016, **16**(11), 1802.

43 A. A. Circuits, *Skin Depth Calculator: EETech Media*, LLC, 2024 [available from: **https://www.allaboutcircuits.com/tools/skin-depth-calculator/**.

44 *Pasternack*, RF Skin Depth Calculator with Formula, 2024 [available from: **https://www.pasternack.com/t-calculator-skin-depth.aspx**.

45 *Thin Film Metamaterial Split Ring Resonators at Microwave Frequencies. 2019 Thirteenth International Congress on Artificial Materials for Novel Wave Phenomena (Metamaterials)*, ed. Paul N., Simon S. K., Bindu C., Andrews J. and Joseph V. P., 16–21 Sept. 2019.

46 B. Camli, E. Altinagac, H. Kizil, H. Torun, G. Dundar and A. D. Yalcinkaya, Gold-on-glass microwave split-ring resonators with PDMS microchannels for differential measurement in microfluidic sensing, *Biomicrofluidics*, 2020, **14**(5), 054102.

47 M. Ho, A. Au, R. Flick, T. V. Vuong, A. A. Sklavounos and I. Swyer, *et al.*, Antifouling Properties of Pluronic and Tetronic Surfactants in Digital Microfluidics, *ACS Appl. Mater. Interfaces*, 2023, **15**(5), 6326–6337.

48 I. Swyer, R. Fobel and A. R. Wheeler, Velocity Saturation in Digital Microfluidics, *Langmuir*, 2019, **35**(15), 5342–5352.

49 A. Ebrahimi, W. Withayachumnankul, S. Al-Sarawi and D. Abbott, High-Sensitivity Metamaterial-Inspired Sensor for Microfluidic Dielectric Characterization, *IEEE Sens. J.*, 2014, **14**(5), 1345–1351.

50 A. Salim and S. Lim, Complementary Split-Ring Resonator-Loaded Microfluidic Ethanol Chemical Sensor, *Sensors*, 2016, **16**(11), 1802.